THE EUROPEAN
PHYSICAL JOURNAL C

Investigating strong gravitational lensing effects by supermassive black holes with Horndeski gravity

Jitendra Kumar[1,a], **Shafqat Ul Islam**[1,b], **Sushant G. Ghosh**[1,2,c]

[1] Centre for Theoretical Physics, Jamia Millia Islamia, New Delhi 110025, India
[2] Astrophysics and Cosmology Research Unit, School of Mathematics, Statistics and Computer Science, University of KwaZulu-Natal, Private Bag 54001, Durban 4000, South Africa

Abstract We study gravitational lensing in strong-field limit by a static spherically symmetric black hole in quartic scalar field Horndeski gravity having additional hair parameter q, evading the no-hair theorem. We find an increase in the deflection angle α_D, photon sphere radius x_{ps}, and angular position θ_∞ that increases more quickly while angular separation s more slowly, but the ratio of the flux of the first image to all other images r_{mag} decreases rapidly with increasing magnitude of the hair q. We also discuss the astrophysical consequences in the supermassive black holes at the centre of several galaxies and note that the black holes in Horndeski gravity can be quantitatively distinguished from the Schwarzschild black hole. Notably, we find that the deviation $\Delta\theta_\infty$ of black holes in Horndeski gravity from their general relativity (GR) counterpart, for supermassive black holes Sgr A* and M87*, for $q = -0.2$, respectively, can reach as much as 2.4227 μas and 1.82026 μas while Δs is about 0.04650 μas for Sgr A* and 0.03493 μas for M87*. The ratio of the flux of the first image to all other images suggest that the Schwarzschild images are brighter than those of the black holes in Horndeski gravity, wherein the deviation $|\Delta r_{mag}|$ is as much as 0.70673. The results suggest that observational tests of hairy black holes in Horndeski gravity are indeed feasible. Taking the supermassive black holes Sgr A* and M87* as the lens, we also compare our hairy Horndeski black holes observable signatures with those of the neutral Horndeski black holes, Galileon black holes and charged Horndeski black holes. It turns out that although it is possible to detect some effects of the strong deflection lensing by the hairy Horndeski black holes and other black holes with the Event Horizon Telescope (EHT) observations, but it is unconvincing to discern these black holes as

deviations are $\mathcal{O}(\mu as)$. We also find that the shadow size is consistent with EHT observation if the deviation parameter $q \in (-0.281979, 0)$

1 Introduction

Gravitational lensing by black holes is one of the most powerful astrophysical tools for investigating the strong-field features of gravity and provide us with information about the distant stars that are too dim to be observed. It can help us detect exotic objects and hence verify alternative theories of gravity. The gravitational lensing theories were developed, among others, by Liebes [1], Refsdal [2], and Bourassa and Kantowski [3]. They have successfully explained the astronomical observations but in the weak field approximation. However, when a lens is a compact object with a photon sphere (such as a black hole), a strong field treatment of gravitational lensing is needed instead because photons passing close to the photon sphere have large deflection angles. Virbhadra and Ellis [4] obtained the lens equation using an asymptotically flat background metric, in the strong-field limit for a Schwarzchild black hole numerically. Apart from the primary and secondary images, they reported two infinite sets of faint relativistic images. An exact lens equation without reference to a background metric was found by Fritelli et al. [5]. Later, Bozza [6] used the strong field limit approximation to obtain analytical expressions for the positions and magnification of the relativistic images and extended his method of lensing for a general class of static and spherically symmetric spacetimes to show that the logarithmic divergence of the deflection angle at photon sphere is a generic feature for such spacetimes. Bozza's [6] methods was extended to several static, spherically symmetric metrics which includes Reissner–Nordström black holes [7], braneworld black holes [8–11], charged black hole of het-

a e-mail: jitendra0158@gmail.com

b e-mail: shafphy@gmail.com (corresponding author)

c e-mails: sghosh2@jmi.ac.in; sgghosh@gmail.com

erotic string theory [12]. The strong gravitational field continues to receive significant attention, more recent works include lensing from other black holes [13–16] and from various modifications of Schwarzschild geometry [17–23], and more recently in $4D$ Einstein-Gauss-Bonnet gravity [24–26]. The gravitational lensing by a primary photon sphere with unstable circular light orbits and by a secondary photon sphere on a wormhole throat in a black-bounce regular spacetime shows the existence of an antiphoton sphere and the formation of infinite images near it [27]. The gravitational lensing received a boost when Event Horizon Telescope (EHT) [28,29] unravelled the first-ever image of the supermassive black hole M87*. These results offer testing grounds for gravity theories on offering a compelling probe of the strong gravitational fields. With this motivation, this paper investigates the strong-field gravitational lensing of light by the hairy black holes in Horndeski gravity [30].

As a modification to GR, the simplest extensions are the scalar–tensor theories like Horndeski gravity [31], probably the most general four-dimensional scalar–tensor theory with equations of motion containing up to second-order derivatives of the dynamical fields. Horndeski theory of gravitation is described by the action principle formulated from the metric and a scalar field that leads to field equations with no derivatives beyond second order for the metric and the scalar field, and the theory has the same symmetries as GR, namely, diffeomorphism and local Lorentz invariance. (see e.g. [32,33]). All the terms present in the action of Horndeski gravity have been shown to be originating from Galileons, i.e. scalar–tensor models having Galilean symmetry in flat spacetime [34]. There are compelling arguments that suggest that certain modifications are required in GR at both very high and very low energy scales. Gravitational collapses are destined to unavoidable singularities, while on cosmological scales, to describe the observed accelerated expansion of the Universe, GR relies on the yet unexplained presence of dark energy [35]. Horndeski theories [36] which have been studied in both the strong gravity on compact objects, such as neutron stars, black holes [37] and in cosmological regimes to describe the accelerated expansion [38]. The space of solutions for Horndeski's theory of gravity is endowed with hairy black holes [39–44], Among the static and spherically symmetric hairy black holes in scalar–tensor theories the simplest case in which solutions admits a hairy profile with a radially dependent scalar field was studied in [41,45–48]. The time-dependent hairy black hole solutions within the Horndeski class of theories have also been obtained [49]. In [50], authors provide a no-hair theorem for static and spherically symmetric black hole solutions with vanishing Galileon hair at infinity which has further examined by Babichev et al. [41] considering Horndeski theories and beyond it. They demon-

strated that shift-symmetric Horndeski theories including the extended ones allow for static and asymptotically flat black holes with a static scalar field [41] such that the Noether current associated with shift symmetry vanishes, while the scalar field cannot be trivial; In turn, it leads to hairy black holes for the quartic Horndeski gravity [41]. Lately, the investigation of black holes in Horndeski and beyond Horndeski theories has received significant attention [30,51–57].

The strong field gravitational lensing effects caused by the charged Galileon black hole [58] was performed by Zhao and Xie [59] and compared with the Schwarzschild black hole, the Reissner–Nordström black hole and the tidal Reissner–Nordström black hole. They found that in specific parameter space, the observables generated by the charged Galileon black hole are close to those given by the tidal black hole. Badía and Eiroa [51] analysed the behaviour as gravitational lenses for the spherically symmetric and asymptotically flat black holes obtained in Horndeski gravity [41]. They found that the lensing effects by a Horndeski black hole are more substantial than in the Schwarzschild case for a specific case. Later, Wang et al. [60] regarded gravitational lensing by the charged Horndeski black hole [43] and also compared with those of the Reissner–Nordström, tidal Reissner–Nordström and charged Galileon black holes, opening a road for distinguishing these black holes.

We investigate the predictions of spherical hairy black holes in quartic Horndeski gravity [30] for the strong-field gravitational lensing effects of supermassive black holes at the center of the Milky Way and other galaxies. Our most exciting result is that the difference between the angular positions of relativistic primary and secondary images in Horndeski gravity and GR could be as large as μas. Also, the calculated values of time delay between these images are different in GR and Horndeski gravity, and the difference could be as significant as seconds. These suggest that observational tests of Horndeski gravity are indeed feasible.

The paper is organized as follows: We begin with briefly reviewing the hairy black holes in Horndeski gravity in the Sect. 2. Restrictions on parameters from the horizon structure and deflection of light is the subject of Sect. 3. Moreover, we also discuss the strong lensing observables by the hairy black holes, including the image positions θ_∞, separation s, magnifications μ_n in Sect. 3. Time delay between the first and second image when they are on the same side of source have been calculated for supermassive black holes SgrA*, M87* and those at the centers of 21 other galaxies in Sect. 4. A numerically analysis of the observables by taking the supermassive black holes NGC 4649, NGC 1332, Sgr A* and M87*, as the lens is part of Sect. 5. Finally, we summarize our results to end the paper in Sect. 6.

We will work in units where $G = c = 1$.

2 Hairy black holes in Horndeski theory of gravity

Horndeski gravity is described by the action formulated from the metric and the scalar field [41]. It involves 4 arbitrary functions Q_i ($i = 2, \ldots 5$) of kinetic term $\chi = -\partial^\mu \phi \partial_\mu \phi / 2$ [41]. Here, we have considered the particular type of the action of [41] which is quartic, i.e, Q_5 term is absent ($Q_5 = 0$). The hairy black hole solution we are interested is derived from the quartic Horndeski gravity [30] whose action reads

$$S = \int d^4x \sqrt{-g} \Big\{ Q_2(\chi) + Q_3(\chi)\Box\phi + Q_4(\chi)R \quad (1)$$

$$+ Q_{4,\chi} [(\Box\phi)^2 - (\nabla^\mu \nabla^\nu \phi)(\nabla_\mu \nabla_\nu \phi)] \Big\}, \quad (2)$$

where $g \equiv \det(g_{\mu\nu})$, $g_{\mu\nu}$ is the metric tensor, R and $G_{\mu\nu}$, respectively, denote Ricci scalar and Einstein tensor. The $\Box$ is the d'Alembert operator and ∇_μ is the covariant derivative. The 4-current vector associated with the Noether charge is [30],

$$j^\nu = \frac{1}{\sqrt{-g}} \frac{\delta S}{\delta(\phi_{,\mu})},$$

which results into

$$\begin{aligned} j^\nu = &-Q_{2,\chi}\, \phi^{,\nu} - Q_{3,\chi}\, (\phi^{,\nu}\Box\phi + \chi^{,\nu}) \\ &- Q_{4,\chi}\, (\phi^{,\nu}R - 2R^{\nu\sigma}\phi_{,\sigma}) \\ &- Q_{4,\chi\,,\chi}\{\phi^{,\nu}[(\Box\phi)^2 - (\nabla_\alpha \nabla_\beta \phi)(\nabla^\alpha \nabla^\beta \phi)] \\ &+ 2(\chi^{,\nu}\Box\phi - \chi_{,\mu}\nabla^\mu\nabla^\nu\phi)\}, \end{aligned} \quad (3)$$

where we have used the usual convention for the Riemann tensor

$$\nabla_\rho \nabla_\beta \nabla_\alpha \phi - \nabla_\beta \nabla_\rho \nabla_\alpha \phi = -R^\sigma_{\ \alpha\rho\beta}\nabla_\sigma\phi. \quad (4)$$

Varying the action (1) with respect to metric tensor $g^{\mu\nu}$ we obtain the field equations [30,41]

$$Q_4 G_{\mu\nu} = T_{\mu\nu}, \quad (5)$$

where

$$\begin{aligned} T_{\mu\nu} = &\frac{1}{2}(Q_{2,\chi}\,\phi_{,\mu}\,\phi_{,\nu} + Q_2 g_{\mu\nu}) + \frac{1}{2}Q_{3,\chi}\,(\phi_{,\mu}\,\phi_{,\nu}\Box\phi \\ &- g_{\mu\nu}\chi_{,\alpha}\,\phi^{,\alpha} + \chi_{,\mu}\,\phi_{,\nu} + \chi_{,\nu}\,\phi_{,\mu}) \\ &- Q_{4,\chi}\Big\{\frac{1}{2}g_{\mu\nu}[(\Box\phi)^2 \\ &- (\nabla_\alpha\nabla_\beta\phi)(\nabla^\alpha\nabla^\beta\phi) - 2R_{\sigma\gamma}\phi^{,\sigma}\phi^{,\gamma}] - \nabla_\mu\nabla_\nu\phi\Box\phi \\ &+ \nabla_\gamma\nabla_\mu\phi\nabla^\gamma\nabla_\nu\phi - \frac{1}{2}\phi_{,\mu}\,\phi_{,\nu}\,R + R_{\sigma\mu}\phi^{,\sigma}\phi_{,\nu} \\ &+ R_{\sigma\nu}\phi^{,\sigma}\phi_{,\mu} + R_{\sigma\nu\gamma\mu}\phi^{,\sigma}\phi^{,\gamma}\Big\} \\ &- Q_{4,\chi\,,\chi}\Big\{g_{\mu\nu}(\chi_{,\alpha}\,\phi^{,\alpha}\Box\phi + \chi_{,\alpha}\chi^{,\alpha}) + \frac{1}{2}\phi_{,\mu}\,\phi_{,\nu} \\ &\times (\nabla_\alpha\nabla_\beta\phi\nabla^\alpha\nabla^\beta\phi - (\Box\phi)^2) - \chi_{,\mu}\,\chi_{,\nu} \end{aligned}$$

$$\begin{aligned} &- \Box\phi(\chi_{,\mu}\,\phi_{,\nu} + \chi_{,\nu}\,\phi_{,\mu}) \\ &- \chi_{,\gamma}\,[\phi^{,\gamma}\nabla_\mu\nabla_\nu\phi - (\nabla^\gamma\nabla_\mu\phi)\phi_{,\nu} - (\nabla^\gamma\nabla_\nu\phi)\phi_{,\mu}]\Big\}. \end{aligned} \quad (6)$$

Henceforth, we shall specialise to a scalar field $\phi \equiv \phi(r)$ [30,41]. It will be the source of a static and spherically symmetric spacetime. The integration of field equations leads to the black hole solution [30]

$$ds^2 = -A(r)dt^2 + B(r)dr^2 + r^2(d\theta^2 + \sin^2\theta d\varphi^2), \quad (7)$$

where

$$A(r) = \frac{1}{B(r)} = 1 - \frac{2m}{r} + \frac{q_o}{r}\ln\left(\frac{r}{2m}\right), \quad (8)$$

where m is the integration constant related to the black hole mass and q_o is a constant that results from Horndeski gravity. The metric (7) represents a hairy black hole in the quartic Horndeski gravity and encompasses the Schwarzschild metric in the limit $q_o \to 0$. The solution (7) is asymptotically flat since $\lim_{r\to\infty} A(r) = 1/B(r) = 1$. The Kretschmann and Ricci scalars diverge [30] along $r = 0$, establishing the metric (7) is scalar polynomial singular.

Indeed, the first exact black hole solution to Horndeski theory, for the vanishing cosmological term, was obtained by Rinaldi [39], wherein the scalar field becomes imaginary in external communication, and the weak energy condition is violated outside the horizon. It was addressed by the inclusion of a cosmological term in action makes it possible to find a black hole with a real scalar field outside [42]. Cisterna and Erices [43] continued in this line and generalize the results [42] by adding a Maxwell term to find flat charged black holes in the Horndeski scenario. Several charged Galileon black holes were obtained by Babichev et al. [58].
The gravitational lensing by the spherically symmetric and asymptotically flat black holes [41] in Horndeski gravity considered to distinguish it from the Reissner–Nordström geometry [51]; the black hole metric reads [41,51]

$$ds^2 = -\left(1 - \frac{2m}{r} - \frac{\tilde{\gamma}}{r^2}\right)dt^2 + \frac{dr^2}{\left(1 - \frac{2M}{r} - \frac{\tilde{\gamma}}{r^2}\right)} + r^2 d\Omega^2, \quad (9)$$

where $\tilde{\gamma} = \tau^2/(2\sigma\xi)$ with $\sigma = M_{pl}^2/16\pi$ and τ, ξ are dimensionless parameters [41,51]. Further, the gravitational lensing by a charged Galileon black hole [58] leads to estimate the observables which can be close to those of a tidal Reissner–Nordström black hole or those of a Reissner–Nordström black hole [59]. The metric of charged Galileon black hole reads [58,59]
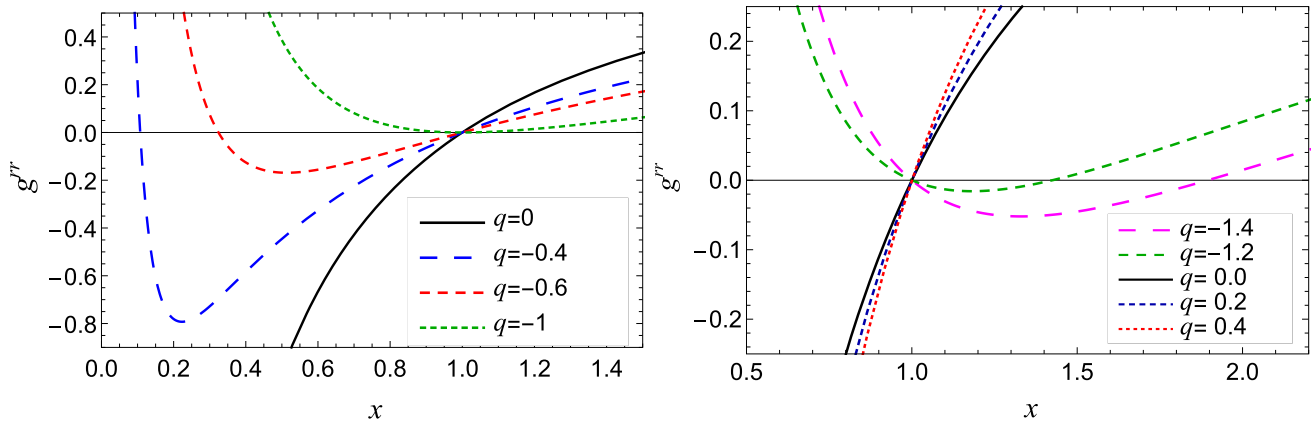
Fig. 1 The horizons of the hairy black hole in Horndeski gravity. When $-\infty < q < 0$ the black hole admits both event horizon x_+ and Cauchy horizon x_-, otherwise has only event horizon for $q > 0$

$$ds^2 = -\left(1 - \frac{2m}{r} + \frac{\tilde{\Gamma}}{r^2}\right)dt^2 + \frac{dr^2}{\left(1 - \frac{2M}{r} + \frac{\tilde{\Gamma}}{r^2}\right)g(r)}$$
$$+ r^2 d\Omega^2, \tag{10}$$

where $g(r) = \left(1 + \frac{\tilde{\Gamma}}{r^2}\right)$ and $\tilde{\Gamma} = (U^2 + V^2)/[2(3\eta v^2 - 2)]$, with U and V being the magnetic and electric charge respectively. v is the linear coefficient of time whereas η indicated the non-minimal kinetic coupling between the scalar field and gravity [58,59]. Also, gravitational lensing by charged black holes from a class of the Horndeski theory when the scalar field coupled only through the Einstein tensor [43] was considered by Wang et al. [43,60]

$$ds^2 = -\left(1 - \frac{2m}{r} + \frac{Q}{r^2} - \frac{Q^2}{12r^4}\right)dt^2$$
$$+ \frac{h(r)dr^2}{\left(1 - \frac{2M}{r} + \frac{Q}{r^2} - \frac{Q^2}{12r^4}\right)} + r^2 d\Omega^2, \tag{11}$$

where $h(r) = \left(1 - \frac{Q}{2r^2}\right)^2$ and Q is the electric charge. It is more complicated than the charged Galileon black hole considered. The charged Horndeski black hole is different from a Reissner–Nordström black hole [43,60].

We shall compare the strong deflection lensing observables by hairy Horndeski black holes and their deviations from the above three black holes viz. by neutral Horndeski black holes, charged Galileon black holes and Charged Horndeski black holes with M87* and Sgr A* as the lens.

3 Strong gravitational lensing by hairy black hole in Horndeski gravity

In this section we shall study gravitational lensing by hairy black hole (7) to investigate how the parameter q_o affects the lensing observables in strong field limit. It should give us useful insights about the possible effects of the parameter q_o on strong gravitational lensing. It is convenient to measure quantities r, q_o, t in terms of the Schwarzschild radius $2m$ [6] and use x instead of r, to rewrite the metric (7) as

$$ds^2 = -A(x)dt^2 + B(x)dx^2$$
$$+ C(x)\left(d\theta^2 + \sin^2\theta d\phi^2\right), \tag{12}$$

where

$$A(x) = \frac{1}{B(x)} = 1 - \frac{1}{x} + \frac{q}{x}\ln(x), \quad C(x) = x^2, \tag{13}$$

and $q = q_o/2m$. For our study of lensing we shall restrict the value of q in the range $-1 \leq q \leq 0$. In addition to curvature scalar polynomial singularity at $x = 0$ the metric (12) is also singular at points where $A(x) = 0$, which are coordinate singularities and the corresponding surfaces are called horizons. In the domain $-1 \leq q < 0$, a simple root analysis of $A(x) = 0$ implies existence of two positive roots ($x_\pm$), corresponding to the Cauchy (x_-) and event horizon (x_+), given by

$$x_- = q \, \text{ProductLog}\left[\frac{\exp(1/q)}{q}\right], \quad x_+ = 1, \tag{14}$$

where ProductLog (z), for arbitrary z, is defined as the principal solution of the equation $w \exp(w) = z$.

The metric (12) always has a horizon at $x = 1$, irrespective of the value of the parameter q. For $0 \leq q < \infty$, the metric (12) has only one horizon namely event horizon fixed at radius $x = 1$ (cf. Fig. 1). For $-1 \leq q < 0$, unlike the Schwarzschild spacetime, it displays two horizons (Cauchy and event) (cf. Fig. 1). The event horizon (x_+) is fixed at the radius $x = 1$, while Cauchy horizon (x_-) increases with decreasing q and merges with the event horizon (x_+) in the limit $q \to -1$ (cf. Fig. 2). Since the metric (12) has curvature singularity at $x = 0$, the existence of horizon for any value of
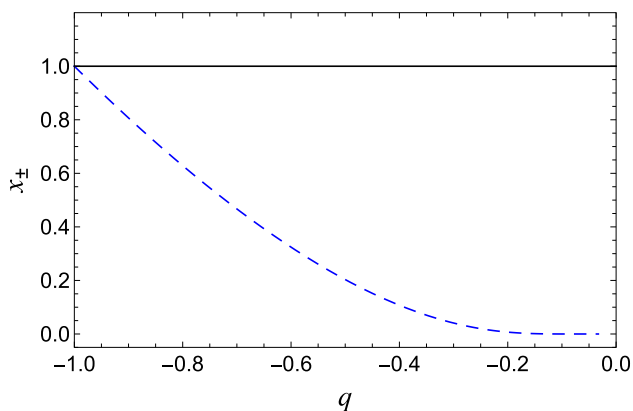
Fig. 2 The event horizon x_+ (solid line) and Cauchy horizon x_- (dashed line) for black holes in Horndeski gravity

q means the cosmic censorship hypothesis [61] is respected for hairy black hole in Horndeski gravity.

The strong field gravitational lensing is governed by deflection angle and lens equation. For this, we first observe that a light-like geodesic of the metric (12) admits two constants of motion, namely the energy $\mathcal{E} = -p_\mu \xi^\mu_{(t)}$ and angular momentum $\mathcal{L} = p_\mu \xi^\mu_{(\phi)}$, where $\xi^\mu_{(t)}$ and $\xi^\mu_{(\phi)}$ are, respectively, the Killing vectors due to time-translational and rotational invariance. The null geodesic equation satisfies $ds^2 = 0$, which gives

$$\left(\frac{dx}{d\tau}\right)^2 \equiv \dot{x}^2 = \mathcal{E}^2 - \frac{\mathcal{L}^2 A(x)}{C(x)}. \tag{15}$$

The static and spherically symmetric compact objects with a strong gravitational field in general relativity have circular photon orbits called photon spheres. The photon sphere being one of the crucial character for strong gravitational lensing [4, 6] does not evolve with time, or in other words, null geodesic initially tangent to the photon sphere hypersurface remains tangent to it. The radius of photon sphere, x_{ps} is the greatest positive solution of the equation [6,16]

$$\frac{C'(x)}{C(x)} = \frac{A'(x)}{A(x)} \implies x_{ps}$$
$$= \frac{3q}{2} \text{ProductLog}\left[\frac{2\exp\left(\frac{1}{3} + \frac{1}{q}\right)}{3q}\right]. \tag{16}$$

From Fig. 4, we observe that when $q \to 0$, we recover the photon sphere radius, $x_{ps} = 1.5$ for the Schwarzschild black hole spacetime [6]. The radial effective potential from Eq. (15), takes the form

$$\frac{V_{\text{eff}}(x)}{\mathcal{E}^2} = \frac{u^2}{x^2}\left[1 - \frac{1}{x} + \frac{q}{x}\ln(x)\right] - 1, \tag{17}$$

which describes different kinds of possible trajectories. By solving $V_{\text{eff}}(x_0) = 0$ and recognising the ratio $\mathcal{L}/\mathcal{E}$ as the impact parameter, we get the expression for impact parameter

u in terms of the closest approach distance x_0 as follows [6]

$$u \equiv \frac{\mathcal{L}}{\mathcal{E}} = \sqrt{\frac{C(x_0)}{A(x_0)}}. \tag{18}$$

Photons, coming from the far distance source, approach the black hole with some impact parameter and get deflected symmetrically to infinity, meanwhile reaching a minimum distance (x_0) near the black hole.

It turns out that light ray exist in the region where $V_{\text{eff}}(x) \leqslant 0$ (cf. Fig. 3). Further, one can define an unstable (or a stable circular orbit) satisfying $V_{\text{eff}}(x) = V'_{\text{eff}}(x) = 0$ and $V''_{\text{eff}}(x_{ps}) < 0$ (or $V''_{\text{eff}}(x_{ps}) > 0$). Next, the first and second derivative of $V_{\text{eff}}(x)$ are

$$\frac{V'_{\text{eff}}(x)}{\mathcal{E}^2} = \frac{u^2}{x^4}[3 + q - 2x - 3q\ln(x)], \tag{19}$$

$$\frac{V''_{\text{eff}}(x)}{\mathcal{E}^2} = -\frac{u^2}{x^5}[12 + 7q - 6x - 12q\ln(x)]. \tag{20}$$

For the hairy black hole in Horndeski gravity we find that $V''_{\text{eff}}(x_{ps}) < 0$, which corresponds to the unstable photon circular orbits (cf. Fig. 3). These photon circular orbits are unstable [62] against small radial perturbations, which would finally drive photons into the black hole or toward spatial infinity.

The deflection angle becomes unboundedly large at $x_0 = x_{ps}$ and is finite only for $x_0 > x_{ps}$. The critical impact parameter u_{ps} is defined as

$$u_{ps} = \sqrt{\frac{C(x_{ps})}{A(x_{ps})}}, \tag{21}$$

and depicted in Fig. 4. The photons with impact parameter $u < u_{ps}$ fall into the black hole, while photons with impact parameter $u > u_{ps}$, reaching the minimum distance x_0 near the black hole, are scattered to infinity. The photons only with impact parameter exactly equal to the critical impact parameter u_{ps} revolve around the black hole in unstable circular orbits and generate a photon sphere of radius x_{ps}.

The deflection angle for the spacetime (12) is given by [6,16]

$$\alpha_D(x_0) = I(x_0) - \pi = 2\int_{x_0}^{\infty} \frac{\sqrt{B(x)}dx}{\sqrt{C(x)}\sqrt{\frac{C(x)A(x_0)}{C(x_0)A(x)} - 1}} - \pi, \tag{22}$$

where x_0 is the closest approach distance of the winding photon. Following Bozza [6,16], we define a variable $z = 1 - x_0/x$ and exploring the relation between the impact parameter u and closest approach distance x_0 in Eq. (18), we find the deflection angle in strong field limit yields
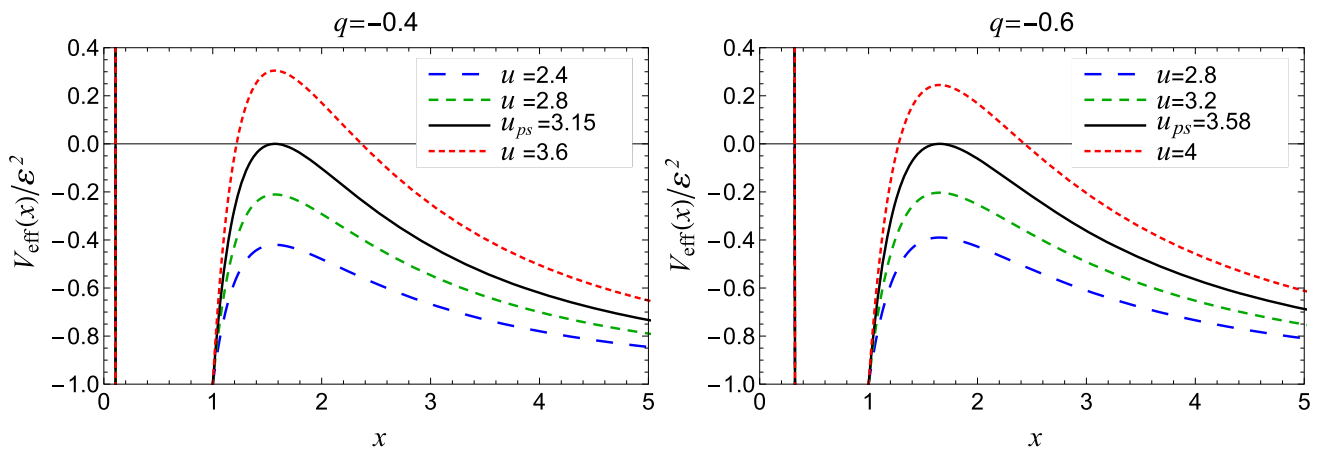
Fig. 3 Variation of the effective potential V_{eff} as a function of radial coordinate x, for different values of q and u. The photons with critical impact parameter (u_{ps}) (black solid curve) make unstable circular orbits

$$\alpha_D(u) = -\bar{a} \log\left(\frac{u}{u_{ps}} - 1\right)$$
$$+ \bar{b} + \mathcal{O}(u - u_{ps}) \log(u - u_{ps}), \tag{23}$$

where $u \approx \theta D_{OL}$. The coefficients $\bar{a}$ and $\bar{b}$ for the case of hairy black hole in Horndeski gravity are given by

$$\bar{a} = \frac{1}{\sqrt{1 + \frac{3}{2}\frac{q}{x_{ps}}}}, $$

$$\bar{b} = -\pi + b_R + \bar{a} \log\left[\frac{2p_2(x_{ps})}{A(x_{ps})}\right], \tag{24}$$

$$b_R = \int_0^1 [R(z, x_{ps}) f(z, x_{ps})$$
$$- R(0, x_{ps}) f_0(z, x_{ps})] dz, \tag{25}$$

$$R(z, x_0) = \frac{2x^2\sqrt{ABC_0}}{x_0 C} = 2, $$

$$f(z, x_0) = \frac{1}{\sqrt{A_0 - A\frac{C_0}{C}}}, \tag{26}$$

$$f_0(z, x_0) = \frac{1}{\sqrt{p_1(x_0)z + p_2(x_0)z^2}}, \tag{27}$$

$$p_1(x_0) = \frac{3q \log(x_0) + 2x_0 - q - 3}{x_0}, \tag{28}$$

$$p_2(x_0) = \frac{-6q \log(x_0) - 2x_0 + 5q + 6}{2x_0}. \tag{29}$$

The deflection angle for the hairy black hole (12) is depicted in Fig. 6, which is monotonically decreasing and $\alpha_D \to \infty$ as $u \to u_{ps}$. When compared with the Schwarzschild black hole (cf. Fig. 6), the deflection angle for the hairy black hole increases with the increasing magnitude of q. A light ray whose u is close enough to u_{ps} can pass close to the photon sphere and go around the lens once, twice, thrice, or many times before reaching the observer. Thus strong gravitational field, in addition to the primary

and secondary images, can give a large number (theoretically an infinite sequence) of images on both sides of the optic axis, which is the line joining the observer and the lens. The two infinite sets of relativistic images correspond to clockwise winding around the black hole and the other produced by counterclockwise winding. When $x_0 \approx x_{ps}$, the coefficient $p_1(x_0)$ vanishes and the leading term of the divergence in $f_0(z, x_0)$ is z^{-1} [6], thus the integral diverges logarithmically. The coefficient b_R is evaluated numerically. The coefficient $\bar{a}$ decreases while $\bar{b}$ increases at first and then, reaching its maximum at $q \approx -0.45$ (cf. Fig. 5), decreases. The coefficients $\bar{a} = 1$ and $\bar{b} = -0.4002$ [6] correspond to the case of the Schwarzschild black hole (cf. Table 1).

The strong deflection limit is adopted for the (approximate) analytic calculations, in which the deflection angle is given by Eq. (23), with the coefficients $\bar{a}$ and $\bar{b}$ depending on the specific form of the metric (Fig. 6). The lens equation geometrically governs the connection between the lens observer and the light source. We assume that the source and observer are far from the black hole (lens) and they are perfectly aligned; the equation for small lensing angle reads [63]

$$\beta = \theta - \frac{D_{LS}}{D_{OS}} \Delta\alpha_n, \tag{30}$$

where $\Delta\alpha_n = \alpha - 2n\pi$ is the offset of deflection angle looping over $2n\pi$ and n is an integer. Here, β and θ are the angular separations between the source and the black hole, and the image and the black hole respectively. D_{OL} and D_{OS} are, respectively, the distance between the observer and the lens and the distance between the observer and the source. Using the Eqs. (23) and (30), the position of the n-th relativistic image can be approximated as [6]

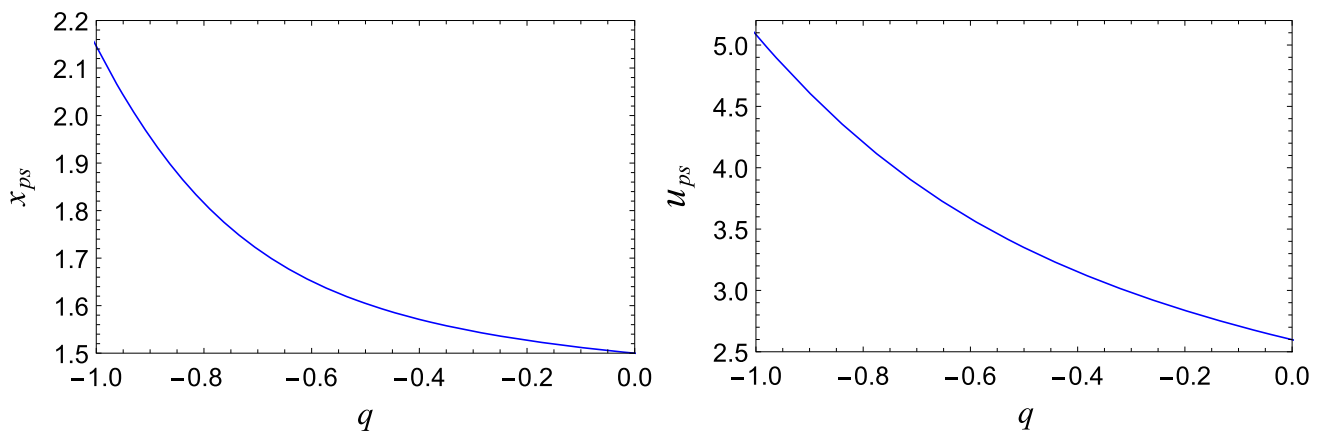$$\theta_n = \theta_n^0 + \frac{u_{ps} e_n(\beta - \theta_n^0) D_{OS}}{\bar{a} D_{LS} D_{OL}}, \tag{31}$$

Fig. 4 The behavior of the photon sphere radius x_{ps} (left) and the critical impact parameter u_{ps} (right) as a function of the hair parameter q. As $q \to 0$, the values $x_{ps} \to 1.5$ and $u_{ps} \to 2.598$ correspond to the Schwarzschild black hole
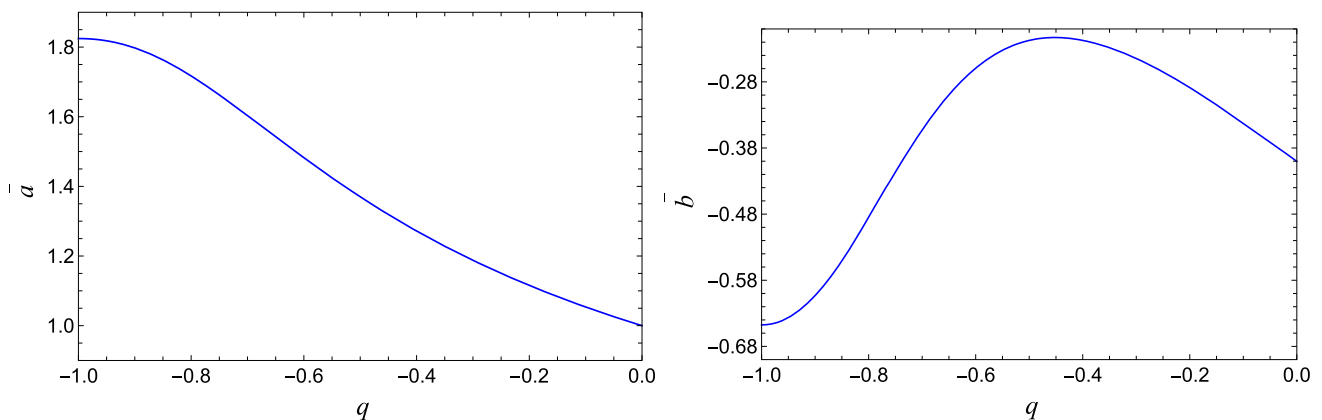

Fig. 5 The behavior of strong lensing coefficients $\bar{a}, \bar{b}$ as a function of the hair parameter q. $\bar{a} = 1$ and $\bar{b} = -0.4002$ at $q = 0$ correspond to the values Schwarzschild black hole

where

$$e_n = \exp\left(\frac{\bar{b} - 2n\pi}{\bar{a}}\right), \tag{32}$$

θ_n^0 are the image positions corresponding to $\alpha = 2n\pi$. As gravitational lensing conserves surface brightness, the magnification is the quotient of the solid angles subtended by the nth image, and the source [4,6,64]. The magnification of nth relativistic image is thus given by [6]

$$\mu_n = \left(\frac{\beta}{\theta} \frac{d\beta}{d\theta}\right)^{-1}\bigg|_{\theta_n^0} = \frac{u_{ps}^2 e_n(1 + e_n)D_{OS}}{\bar{a}\beta D_{LS} D_{OL}^2}. \tag{33}$$

The first relativistic image is the brightest one, and the magnifications decrease exponentially with n. The magnifications are proportional to $1/D_{OL}^2$, which is a very small factor and thus the relativistic images are very faint, unless β has values close to zero, i.e. nearly perfect alignment.

If θ_∞ represents the asymptotic position of a set of images in the limit $n \to \infty$, we consider that only the outermost image θ_1 is resolved as a single image and all the remain-

Table 1 Estimates for the strong lensing coefficients $\bar{a}, \bar{b}$ and the critical impact parameter u_{ps}/R_s for the hairy black hole in Horndeski gravity. The values at $q = 0$ corresponds to the Schwarzschild black hole. $\bar{a}, \bar{a}$ are dimensionless whereas u_m is in the units of Schwarzschild radius $R_s = 2GM/c^2$

q	Lensing coefficients		
	$\bar{a}$	$\bar{b}$	u_{ps}/R_s
0	1.0000	-0.40023	2.59808
-0.2	1.11557	-0.289002	2.83714
-0.4	1.27196	-0.217103	3.15179
-0.6	1.48241	-0.259327	3.58493
-0.8	1.71709	-0.484924	4.20506
-1.0	1.82457	-0.647521	5.0838

ing ones are packed together at θ_∞. Having obtained the deflection angle (23) and lens equation (30) we calculate three observables of relativistic images (cf. Table 2), angular position of the asymptotic relativistic images (θ_∞), angular
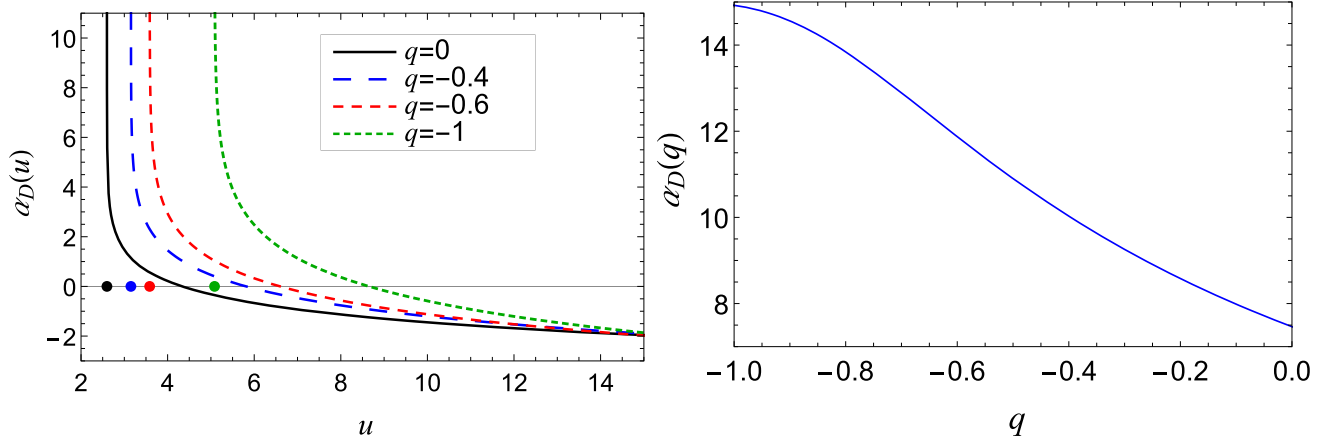
Fig. 6 **a** (Left) The Variation of deflection angle as a function of impact parameter u for different values of the parameter q. Points on the horizontal axis represent the values of the impact parameter $u = u_{ps}$ at which the deflection angle diverges. **b** (Right) Deflection angles evaluated at $u = u_{ps} + 0.001$ as function of the parameter q
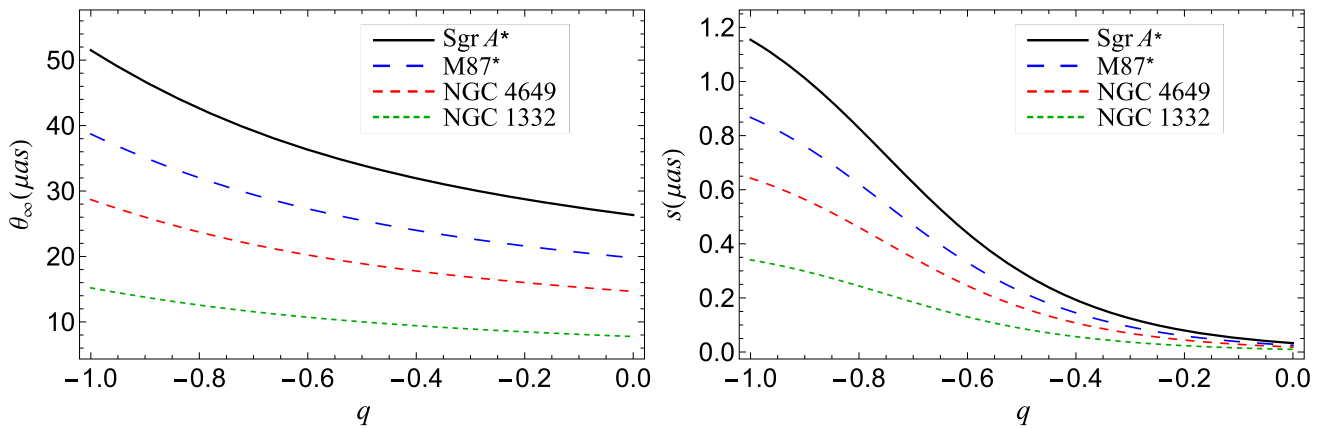

Fig. 7 The behavior of lensing observables θ_∞ (left), s (right) as a function of hair parameter q in strong field limit by considering the supermassive black holes at the centres of nearby galaxies as hairy black holes in Horndeski gravity

Table 2 Estimates for the lensing observables of primary images for black holes in Horndeski gravity and compared with Schwarzschild black ($q = 0$) in GR considering the supermassive black holes Sgr A*, M87*, NGC 4649, and NGC 1332 as lens. The observable r_{mag} does not depend upon the mass or distance of the black hole from the observer

q	Sgr A*		M87*		NGC 4649		NGC 1332		r_{mag}
	$\theta_\infty(\mu as)$	$s(\mu as)$	$\theta_\infty(\mu as)$	$s(\mu as)$	$\theta_\infty(\mu as)$	$s(\mu as)$	$\theta_\infty(\mu as)$	$s(\mu as)$	
0.0	26.3299	0.0329517	19.782	0.0247571	14.6615	0.0183488	7.76719	0.00972061	6.82188
-0.2	28.7526	0.0794533	21.6023	0.0596944	16.0106	0.0442427	8.4819	0.0234384	6.11514
-0.4	31.9414	0.192717	23.998	0.144791	17.7862	0.107312	9.42256	0.0568506	5.36327
-0.6	36.331	0.440102	27.296	0.330656	20.2305	0.245066	10.7175	0.129828	4.60187
-0.8	42.6156	0.827456	32.0177	0.62168	23.7301	0.46076	12.5714	0.244096	3.97294
-1.0	51.5211	1.15426	38.7086	0.867213	28.689	0.642738	15.1985	0.340502	3.73889

separation between the outermost and asymptotic relativistic images (s) and relative magnification of the outermost relativistic image with other relativistic images (r_{mag}) [6,65]

$$\theta_{\infty} = \frac{u_{ps}}{D_{OL}}, \tag{34}$$

$$s = \theta_1 - \theta_{\infty} = \theta_{\infty} \exp\left(\frac{\bar{b}}{\bar{a}} - \frac{2\pi}{\bar{a}}\right), \tag{35}$$

$$r_{\text{mag}} = \frac{5\pi}{\bar{a}\log(10)}. \tag{36}$$

The strong deflection limit coefficients $\bar{a}$, $\bar{b}$ and the critical impact parameter u_{ps} can be obtained after measuring s, r_{mag} and θ_{∞}. Then, comparing their values with those predicted by the theoretical models, we can identify the nature of the hairy black holes (lens).

4 Time delay in strong field limit

The time difference is caused by the photon taking different paths while winding the black hole, so there is a time delay between different images, which generally depends upon which side of the lens, the images are formed. If we can distinguish the time signals of the first image and other packed images, we can calculate the time delay of two signals [66]. The time spent by the photon winding the black is given by [66]

$$\tilde{T}(u) = \tilde{a}\log\left(\frac{u}{u_{ps}} - 1\right) + \tilde{b} + \mathcal{O}(u - u_{ps}). \tag{37}$$

The images are highly demagnified, and the separation between the images is of the order of μas, so we must at least distinguish the outermost relativistic image from the rest, and we assume the source to be variable, which generally are abundant in all galaxies, otherwise, there is no time delay to measure. The time delay when two images are on the same side is [66]

$$\Delta T_{n,m}^{s} = 2\pi(n-m)\frac{\tilde{a}}{\bar{a}} + 2\sqrt{\frac{B(x_{ps})u_{ps}}{A(x_{ps})c}}$$
$$\times \left[\exp\left(\frac{\bar{b} - 2m\pi \pm \beta}{2\bar{a}}\right) - \exp\left(\frac{\bar{b} - 2n\pi \pm \beta}{2\bar{a}}\right)\right]. \tag{38}$$

The upper sign before β signifies that both the images are on the same side of the source and the lower sign if the images are on the other side. When the images are on the opposite sides of lens, the time dilation between mth and nth relativistic image is give

$$\Delta T_{n,m}^{o} = [2\pi(n-m) - 2\beta]\frac{\tilde{a}}{\bar{a}} + 2\sqrt{\frac{B(x_{ps})u_{ps}}{A(x_{ps})c}}$$
$$\times \left[\exp\left(\frac{\bar{b} - 2m\pi + \beta}{2\bar{a}}\right) - \exp\left(\frac{\bar{b} - 2n\pi + \beta}{2\bar{a}}\right)\right]. \tag{39}$$

The contribution of second term in Eqs. (38) and (39) is very small. For spherically symmetric black holes, the time delay between the first and second relativistic image is given by

$$\Delta T_{2,1}^{s} = 2\pi u_{ps} = 2\pi D_{OL}\theta_{\infty}. \tag{40}$$

Using Eq. (40), if we can measure the time delay with an accuracy of 5% and critical impact parameter with negligible error, we can get the distance of the black hole with an accuracy of 5%. In Table 3, we compare the values of time delay between the first and second relativistic image considering the black hole at the center of several nearby galaxies to be Schwarzschild black hole and hairy black hole in Horndeski gravity at $q = -0.5$.

5 Gravitational lensing parameters for supermassive black holes

The EHT collaboration has revealed the first direct image of the black hole M87*, which is as per the shadow of a Kerr black hole of general relativity, i.e., it may not be as per a nonrotating black hole [28]. The inferred size of the shadow of M87* and the inferred circularity deviation $\Delta C \leq 10\%$ for the M87* black hole agree with the prediction based on a Kerr black hole. However, this deviation from the circularity of the shadow happens when the black hole is rapidly rotating spin $a \approx 1$, i.e., the shadow cast by rotating black holes is more or less circular when a takes a smaller value [67–69]. As shown in Ref. [70], the constraints on the a in the modified theories of gravity shadow are only slightly changing when the nonrotating hairy metrics are used. One can also use the EHT observation results to test these nonrotating hairy black holes. Hence, we model the supermassive black holes in the nearby galaxies especially Sgr A*, M87*, NGC4649 and NGC1332 as the hairy black hole to estimate and compare the observables with those of Schwarzschild black hole of GR.

Using Eq. (30), we compute the angular positions for first and second order relativistic primary and secondary images; the images on the same and opposite sides of the source respectively, taking $d = D_{LS}/D_{OS} = 0.5$, for Sgr A* and M87* black holes. First (Second) order relativistic images are produced after the light winds, once (twice) around the black hole before reaching the observer. From the results in Tables 4 and 5 it shows that in the Horndeski gravity the angular positions of images are larger than their corresponding values in GR and are very insensitive to the position of

Table 3 Estimation of time delay for supermassive black holes at the center of nearby galaxies in the case Schwarzschild and hairy black holes in Horndeski gravity ($q = -0.5$). Mass (M) and distance (D_{OL}) are given in the units of solar mass and Mpc, respectively. Time Delays are expressed in minutes

Galaxy	$M(M_\odot)$	D_{OL} (Mpc)	M/D_{OL}	$\Delta T_{2,1}^s$ (Schw.)	$\Delta T_{2,1}^s$ (Hairy)
Milky Way	4.3×10^6	0.0083	2.471×10^{-11}	11.4968	14.8236
M87	6.15×10^9	16.68	1.758×10^{-11}	16443.1	21201.2
NGC 4472	2.54×10^9	16.72	7.246×10^{-12}	6791.11	8756.28
NGC 1332	1.47×10^9	22.66	3.094×10^{-12}	3930.29	5067.61
NGC 4374	9.25×10^8	18.51	2.383×10^{-12}	2473.14	3188.8
NGC 1399	8.81×10^8	20.85	2.015×10^{-12}	2355.5	3037.12
NGC 3379	4.16×10^8	10.70	1.854×10^{-12}	1112.25	1434.1
NGC 4486B	6×10^8	16.26	1.760×10^{-12}	1604.2	2068.41
NGC 1374	5.90×10^8	19.57	1.438×10^{-12}	1577.46	2033.94
NGC 4649	4.72×10^9	16.46	1.367×10^{-12}	12619.7	16271.5
NGC 3608	4.65×10^8	22.75	9.750×10^{-13}	1243.26	1603.02
NGC 3377	1.78×10^8	10.99	7.726×10^{-13}	475.913	613.629
NGC 4697	2.02×10^8	12.54	7.684×10^{-13}	540.081	696.365
NGC 5128	5.69×10^7	3.62	7.498×10^{-13}	152.132	196.154
NGC 1316	1.69×10^8	20.95	3.848×10^{-13}	451.85	582.603
NGC 3607	1.37×10^8	22.65	2.885×10^{-13}	366.292	472.287
NGC 4473	0.90×10^8	15.25	2.815×10^{-13}	240.63	310.262
NGC 4459	6.96×10^7	16.01	2.073×10^{-13}	186.087	239.936
M32	2.45×10^6	0.8057	1.450×10^{-13}	6.55048	8.44601
NGC 4486A	1.44×10^7	18.36	3.741×10^{-14}	38.5008	49.6419
NGC 4382	1.30×10^7	17.88	3.468×10^{-14}	34.7577	44.8156
CYGNUS A	2.66×10^9	242.7	1.4174×10^{-15}	7111.95	9169.96

Table 4 Image positions of first and second order primary and secondary images due to lensing by Sgr A* with $d = D_{LS}/D_{OS} = 0.5$: GR and Horndeski Gravity ($q = -0.5$) predictions for angular positions θ of primary (p) and secondary images (s) are given for different values of angular source position β. **(a)** All values of θ are in μas. **(b)** We have used $M_{\text{Sgr A*}} = 4.3 \times 10^6 \, M_\odot$, $D_{OL} = 8.3 \times 10^6$ pc

$\beta(as)$	Horndeski gravity				General relativity			
	$\theta_{1p,\text{HG}}$	$\theta_{2p,\text{HG}}$	$\theta_{1s,\text{HG}}$	$\theta_{2s,\text{HG}}$	$\theta_{1p,\text{GR}}$	$\theta_{2p,\text{GR}}$	$\theta_{1s,\text{GR}}$	$\theta_{2s,\text{GR}}$
0	34.2444	33.952	-34.2444	-33.952	26.3628	26.3299	-26.3628	-26.3299
10^0	34.2444	33.952	-34.2444	-33.952	26.3628	26.3299	-26.3628	-26.3299
10^1	34.2445	33.952	-34.2444	-33.952	26.3628	26.3299	-26.3628	-26.3299
10^2	34.2446	33.952	-34.2442	-33.952	26.3628	26.3299	-26.3628	-26.3299
10^3	34.2465	33.952	-34.2423	-33.952	26.3631	26.3299	-26.3625	-26.3299
10^4	34.2653	33.9522	-34.2235	-33.9518	26.366	26.3299	-26.3596	-26.3299

Table 5 Image positions of first and second order primary and secondary images due to lensing by M87* with $d = D_{LS}/D_{OS} = 0.5$: GR and Horndeski Gravity ($q = -0.5$) predictions for angular positions θ of primary (p) and secondary images (s) are given for different values of angular source position β. **(a)** All values of θ are in μas. **(b)** We have used $M_{\text{M87*}} = 6.5 \times 10^9 \, M_\odot$, $D_{OL} = 16.8 \times 10^6$ pc

$\beta(as)$	Horndeski gravity				General relativity			
	$\theta_{1p,\text{HG}}$	$\theta_{2p,\text{HG}}$	$\theta_{1s,\text{HG}}$	$\theta_{2s,\text{HG}}$	$\theta_{1p,\text{GR}}$	$\theta_{2p,\text{GR}}$	$\theta_{1s,\text{GR}}$	$\theta_{2s,\text{GR}}$
0	25.7284	25.5087	-25.7284	-25.5087	19.8068	19.7821	-19.8068	-19.7821
10^0	25.7284	25.5087	-25.7284	-25.5087	19.8068	19.7821	-19.8068	-19.7821
10^1	25.7284	25.5087	-25.7283	-25.5087	19.8068	19.7821	-19.8068	-19.7821
10^2	25.7285	25.5087	-25.7282	-25.5087	19.8068	19.7821	-19.8068	-19.7821
10^3	25.7299	25.5087	-25.7268	-25.5086	19.807	19.7821	-19.8065	-19.7821
10^4	25.7441	25.5088	-25.7127	-25.5085	19.8092	19.7821	-19.8044	-19.7821

Table 6 Magnifications of first order and second order relativistic images due to lensing by Sgr A* with $d = D_{LS}/D_{OS} = 0.5$: GR and Horndeski Gravity ($q = -0.5$) predictions for magnifications μ_n is given for different values of angular source position β. **(a)** $1p$ and $1s$ refer to first order relativistic images on the same side as primary and secondary images, respectively. **(b)** We have used $M_{Sgr\,A*} = 4.3 \times 10^6$ m, $D_{OL} = 8.3 \times 10^6$ pc **(c)** Angular positions of first order relativistic images in GR and Horndeski Gravity are, respectively, $\theta_{1p,GR} \approx -\theta_{1s,GR} \approx 26.3628\mu as$ and $\theta_{1p,HG} \approx -\theta_{1s,HG} \approx 34.244\mu as$ and are highly insensitive to the angular source position β

β	Horndeski gravity				General relativity			
	$\mu_{1p,HG}$	$\mu_{2p,HG}$	$\mu_{1s,HG}$	$\mu_{2s,HG}$	$\mu_{1p,GR}$	$\mu_{2p,GR}$	$\mu_{1s,GR}$	$\mu_{2s,GR}$
10^0	7.2458×10^{-11}	7.32635×10^{-13}	-7.2458×10^{-11}	-7.32635×10^{-13}	8.52495×10^{-12}	1.59×10^{-14}	-8.52495×10^{-12}	-1.59×10^{-14}
10^1	7.2458×10^{-12}	7.32635×10^{-14}	-7.2458×10^{-12}	-7.32635×10^{-14}	8.52495×10^{-13}	1.59×10^{-15}	-8.52495×10^{-13}	-1.59×10^{-15}
10^2	7.2458×10^{-13}	7.32635×10^{-15}	-7.2458×10^{-13}	-7.32635×10^{-15}	8.52495×10^{-14}	1.59×10^{-16}	-8.52495×10^{-14}	-1.59×10^{-16}
10^3	7.2458×10^{-14}	7.32635×10^{-16}	-7.2458×10^{-14}	-7.32635×10^{-16}	8.52495×10^{-15}	1.59×10^{-17}	-8.52495×10^{-15}	-1.59×10^{-17}
10^4	7.2458×10^{-15}	7.32635×10^{-17}	-7.2458×10^{-15}	-7.32635×10^{-17}	8.52495×10^{-16}	1.59×10^{-18}	-8.52495×10^{-16}	-1.59×10^{-18}

Table 7 Magnifications of first and second order relativistic images due to lensing by M87* with $d = D_{LS}/D_{OS} = 0.5$: GR and Horndeski Gravity ($q = -0.5$) predictions for magnifications μ_n is given for different values of angular source position β. **(a)** $1p$ and $1s$ refer to first order relativistic images on the same side as primary and sec- ondary images, respectively. **(b)** We have used $M_{M87*} = 6.5 \times 10^9$ m, $D_{OL} = 16.8 \times 10^6$ pc **(c)** Angular positions of first order relativistic images in GR and Horndeski Gravity are, respectively, $\theta_{1p,GR} \approx -\theta_{1s,GR} \approx 19.8068\mu as$ and $\theta_{1p,HG} \approx -\theta_{1s,HG} \approx 25.7284\mu as$ and are highly insensitive to the angular source position β

β	Horndeski gravity				General relativity			
	$\mu_{1p,HG}$	$\mu_{2p,HG}$	$\mu_{1s,HG}$	$\mu_{2s,HG}$	$\mu_{1p,GR}$	$\mu_{2p,GR}$	$\mu_{1s,GR}$	$\mu_{2s,GR}$
10^0	4.04123×10^{-11}	4.08616×10^{-13}	-4.04123×10^{-11}	-4.08616×10^{-13}	4.75466×10^{-12}	8.86797×10^{-15}	-4.75466×10^{-12}	-8.86797×10^{-15}
10^1	4.04123×10^{-12}	4.08616×10^{-14}	-4.04123×10^{-12}	-4.08616×10^{-14}	4.75466×10^{-13}	8.86797×10^{-16}	-4.75466×10^{-13}	-8.86797×10^{-16}
10^2	4.04123×10^{-13}	4.08616×10^{-15}	-4.04123×10^{-13}	-4.08616×10^{-15}	4.75466×10^{-14}	8.86797×10^{-17}	-4.75466×10^{-14}	-8.86797×10^{-17}
10^3	4.04123×10^{-14}	4.08616×10^{-16}	-4.04123×10^{-14}	-4.08616×10^{-16}	4.75466×10^{-15}	8.86797×10^{-18}	-4.75466×10^{-15}	-8.86797×10^{-18}
10^4	4.04123×10^{-15}	4.08616×10^{-17}	-4.04123×10^{-15}	-4.08616×10^{-17}	4.75466×10^{-16}	8.86797×10^{-19}	-4.75466×10^{-16}	-8.86797×10^{-19}

the source β. The angular positions $\theta_{1p} > |\theta_{1s}|$ for higher values of β, however, for small values of β the values are extremely close. The same is true for any pair of second or higher order relativistic images. In Horndeski gravity the first and second order primary images are about 7.8 and 7.6 μas larger than their corresponding values in GR at $q = -0.5$, an effect too tiny to be observed with today's telescopes, especially since these relativistic images are highly demagnified. However the deviation becomes significant at higher magnitude of q and the next generation telescope (ngEHT) which renders these observables, the deviations could be used to test Horndeski gravity.

The characteristic observables which include position of the innermost image θ_∞ and the separation s, are depicted in Fig. 7 and tabulated in Table 2. Considering the Sgr A* and M87* as the lens we find that these observables vary rapidly with parameter q; with θ_∞ ranging in between 26.33 and 51.52 μas for Sgr A* and 19.78 and 38.71 μas for M87* and the latter are consistent with the EHT measured diameters of M87* shadow 42 ± 3 μas. The deviation from their GR counterpart are quite significant and can reach as much as 25.1912 μas for Sgr A* and 18.92μas for M87*. Further, the separation s due to hairy black holes for Sgr A* and M87* range between 0.0329 and 1.15426 μas and 0.024 and 0.867 μas, respectively. We also obtain these results for
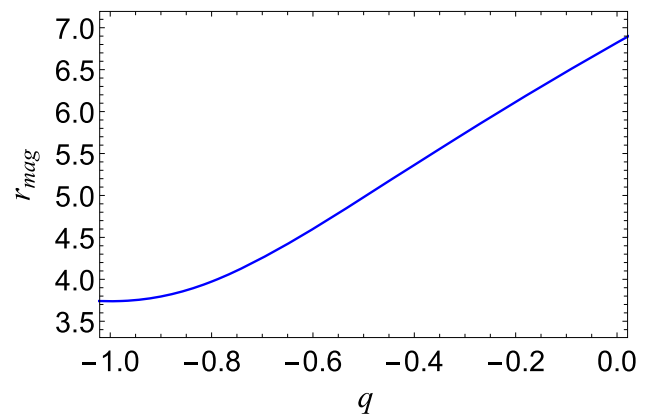
Fig. 8 The behavior of strong lensing observable r_{mag} as function of the parameter q. It is independent of the black holes mass or its distance from the observer

NGC 4649 and NGC 1332 and found that the deviation is also of the order of $\mathcal{O}(\mu)as$. As the deviation of position of the images are quite significant at higher magnitude of q and these images could be resolved, it is possible to measure the brightness difference. The relative magnification of the first and second order images of Tables 4 and 5 are tabulated in Tables 6 and 7 using Eq. (33) for black holes in GR and Horndeski gravity at ($q = -0.5$). The first order images
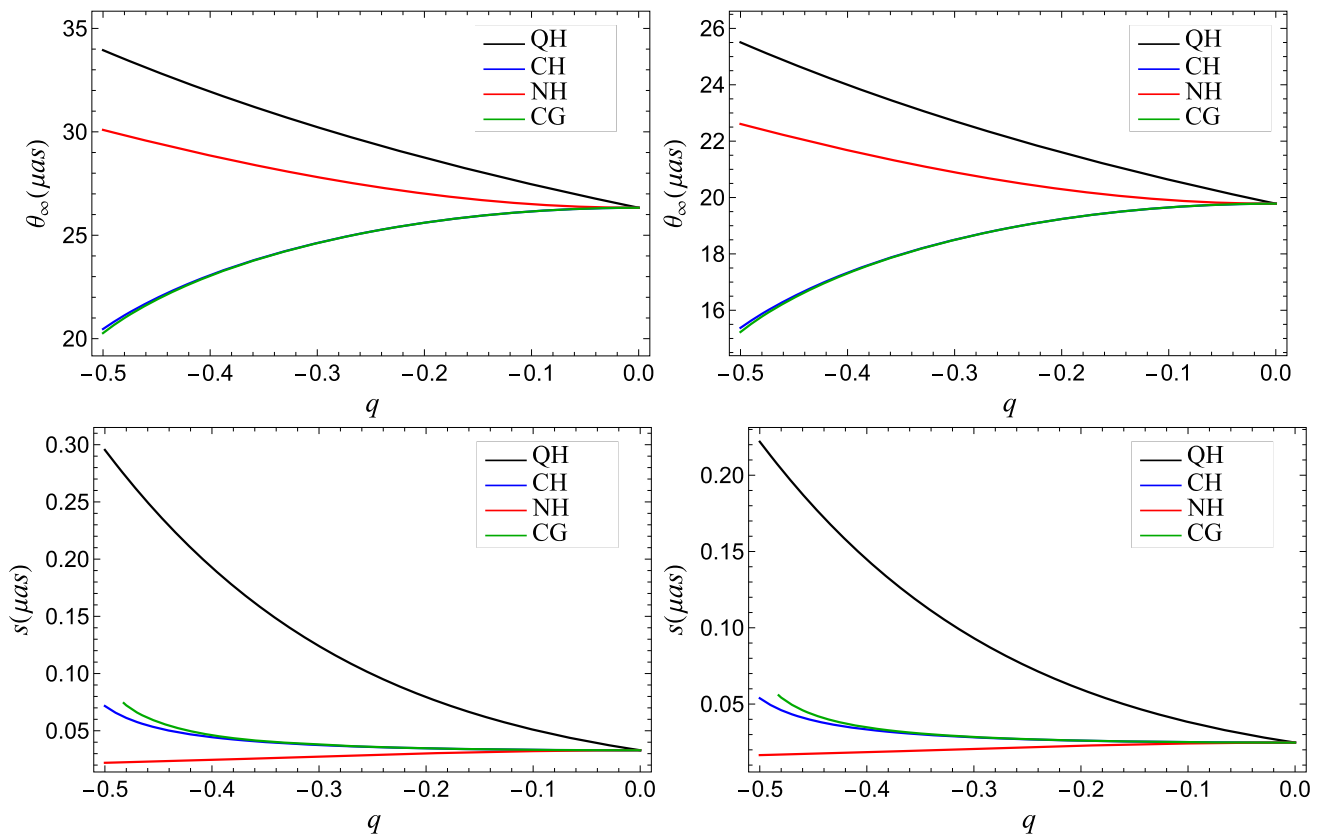
Fig. 9 The behaviour of lensing Observables θ_∞, s for quartic Horndeski black holes (QH), charged Horndeski black holes (CH), Horndeski black holes (NH) and charged Galilleon black holes (CG) with q by modelling them as Sgr A* black hole (left) and M87* black hole (right). The parameter q is q_e, γ and Γ for charged Horndeski black holes, Horndeski black holes and charged Galilleon black holes, respectively

in Horndeski gravity are highly magnified than the second order images as well the corresponding images in GR. However, the ratio of the flux of the first image to the all other images rapidly decreases with decreasing q implying that the Schwarzschild images are brighter than the hairy black holes in Horndeski gravity (cf. Fig. 8). We have also depicted the differences between the quartic Horndeski black holes (12) from those of charged Horndeski black holes [60], Horndeski black holes [51] and charged Galileon black holes [59] in Fig. 9 for Sgr A* and M87* (see also, Table 8). We have measured all the distances in terms of Schwarzschild radius and used, respectively, $q_e^2 = Q/(4M^2)$, $\gamma^2 = \tilde{\gamma}/(4M^2)$ and $\Gamma^2 = \tilde{\Gamma}/(4M^2)$ for charged Horndeski black holes, Horndeski black holes, charged Galileon black holes. The charged Galileon black holes are indistinguishable from the charged Horndeski black holes, for most of the values of q (cf. Fig. 9). In general, these three black holes, are potentially different from those of quartic Horndeski black holes. For a given negative value of q, the quartic Horndeski black hole possesses

the largest values of θ_∞ and s. Contrary to these observables, the brightness difference r_{mag} is smallest for the quartic Horndeski black hole (cf. Fig. 10). The observables of quartic Horndeski black holes deviate from the three black holes (cf. Figs. 9, 10), but the absolute deviation is of $\mathcal{O}(\mu as)$ when $-0.4 < q < 0$ (cf. Table 9). For large q, the deviation of θ_∞ could be more than $10\mu as$ but this value of q is not allowed by EHT observation of M87*. Finally, we use fourteen supermassive black holes, which considerably differ from Sgr A* and M87*, to calculate the time delays between the first and second-order relativistic primary images $\Delta T_{2,1}^s$ in Table 3. For Sgr A* and M87*, the time delay can reach ~ 14.82 min and ~ 21201.2 min at $q = -0.5$ and hence deviate from their corresponding black hole in GR by ~ 3.32 min and ~ 4758.1 min. Although these deviations are insignificant for Sgr A* but for M87* and other black holes, these are sufficient values to test and compare the Horndeski gravity from GR.

Table 8 The lensing Observables θ_∞, s, r_{mag}, lensing coefficients $\bar{a}$, $\bar{b}$ and critical impact parameter u_m for QH, CH, NH and CG by modelling them as Sgr A* and M87* black holes. r_{mag}, $\bar{a}$, $\bar{b}$ are dimensionless whereas u_m is in the units of Schwarzschild radius $R_s = 2GM/c^2$

	QH		CH		NH		CG	
	$q = -0.1$	$q = -0.2$	$q_e = -0.1$	$q_e = -0.2$	$\gamma = -0.1$	$\gamma = -0.2$	$\Gamma = -0.1$	$\Gamma = -0.2$
Sgr A*								
$\theta_\infty(\mu\mathrm{as})$	27.4645	28.7526	26.153	25.6056	26.5041	27.0114	26.1529	25.6044
$s(\mu\mathrm{as})$	0.0510219	0.0794533	0.0333325	0.0346314	0.0321872	0.0301558	0.033335	0.0346784
M87*								
$\theta_\infty(\mu\mathrm{as})$	20.6345	21.6023	19.6492	19.2378	19.9129	20.2941	19.6491	19.2369
$s(\mu\mathrm{as})$	0.0383335	0.0596944	0.0250432	0.0260191	0.0241827	0.0226565	0.0250451	0.0260544
r_{mag}	6.47466	6.11514	6.80639	6.75556	6.85161	6.93431	6.806289	6.75366
u_m/R_s	2.71004	2.83714	2.58063	2.52661	2.61526	2.66533	2.580619	2.52649
$\bar{a}$	1.05363	1.11557	1.00228	1.00982	0.995661	0.983787	1.00229	1.0101
$\bar{b}$	-0.342441	-0.289002	-0.397167	-0.387468	-0.40117	-0.404246	-0.397192	-0.387932

Table 9 The lensing observables θ_∞, s and r_{mag} for QH, CH, NH and CG at $q = -0.139322$ and Schwarzschild black hole (SC) by modelling them as Sgr A* and M87*. The deviation of these black holes (BHs) from quartic Horndeski black hole at $q = -0.139322$ have also been calculated where $\delta(\langle\mathrm{BH}\rangle) = X_{\mathrm{QH}} - X_{\langle\mathrm{BH}\rangle}$ with $\langle\mathrm{BH}\rangle = \mathrm{SC}$, CH, NH, CG

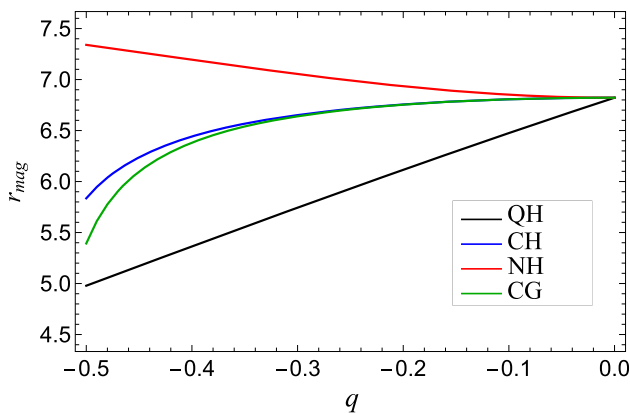|	QH	SC	δ(SC)	CH	δ(CH)	NH	δ(NH)	CG	δ(CG)
Sgr A*									
$\theta_\infty(\mu\mathrm{as})$	27.95099	26.32986	1.621128	25.9841	1.966896	26.66559	1.285399	25.98384	1.967157
$s(\mu\mathrm{as})$	0.060697	0.032951	0.027745	0.033713	0.0269838	0.0315101	0.0291868	0.0337230	0.0269739
M87*									
$\theta_\infty(\mu\mathrm{as})$	21.00	19.782	1.217978	19.52224	1.477758	20.03426	0.965739	19.52205	1.477955
$s(\mu\mathrm{as})$	0.0456025	0.024757	0.020845	0.0253292	0.0202733	0.0236740	0.0219285	0.025336	0.0202659

Fig. 10 The behavior of strong lensing observable r_{mag} for quartic Horndeski black holes (QH), charged Horndeski black holes (CH), Horndeski black holes (NH) and charged Galilleon black holes (CG). The parameter q is q_e, γ and Γ for charged Horndeski black holes, Horndeski black holes and charged Galilleon black holes, respectively

5.1 Constraint on the parameter q from EHT observations of M87*

The EHT observation unveiled event-horizon-scale images of the supermassive black hole M87* as an asymmetric bright emission ring with a size of a diameter of 42 ± 3 μas, and it is consistent with the shadow of a Kerr black hole of general relativity. The EHT data indicated a mass for the M87* black hole of $(6.5 \pm 0.7) \times 10^9 M_\odot$. It offers a new and powerful gravitational test of the black-hole metric in the strong-field regime [70].

The spacetimes that deviate from the Kerr metric can lead to significant deviations in the predicted black-hole shadows inconsistent with even the current EHT measurements. The shadow-size measurements place significant constraints on deviation parameters that control each black hole metric [70–73]. The EHT observation disfavors a nonrotating black hole M87*, and the inferred size of the shadow of M87* is indeed consistent with the prediction based on a Kerr black hole. However, the size of the black-hole shadow both in the Kerr metric and in other parametric extensions depends very weakly on the black-hole spin [67,70]. It turns out that the constraints on the parameters in the modified theories of gravity deduced EHT observations do have slight change for the nonrotating metrics [70]. Thereby, the EHT observation can also be adopted to test these hairy black holes in the Horedenski theory appropriately. The observables in the strong deflection gravitational lensing contain the apparent

radius of the photon sphere (the angular size of the shadow) θ_∞. Taking M87* as the lens with EHT observation, we find its observable θ_∞ for the hairy black holes in the Horndeski theory and find that the angular radius of the shadows θ_∞ range from 19.86271 μas $< \theta_\infty <$ 25.5064 μas only when $-0.5 < q < 0.0$. Indeed, we find that 39 μas $< 2\theta_\infty <$ 45 μas only when $-0.281979 < q < 0.0$, i.e., the measured diameter 42 ± 3 μas of the M87* shadow by EHT constraint the parameter q, and for $q = -0.139322$, we find that $2\theta_\infty = 42$ μas. Thus, requiring that the shadow size is consistent to within 1σ bound, the 2017 EHT observation for M87* places a bound on the deviation parameter q.

6 Conclusion

One of the most renowned scalar–tensor theories is Horndeski gravity, in which scalar fields constitute additional degrees of freedom and is the most general four-dimensional scalar–tensor theory with equations of motion containing second-order derivatives of the dynamical fields. We have investigated gravitational lensing effects of spherically symmetric hairy black holes in Horndeski gravity having additional parameter q and also consider the predictions of Horndeski gravity for lensing effects by supermassive black holes Sgr A*, M87* and 21 others in comparison with GR. We examined the effect of the parameter q on the light deflection angle α_D, strong lensing coefficients $\bar{a}$, $\bar{b}$ and lensing observables $\theta_\infty, s, r_{\mathrm{mag}}, u_{ps}$ and time delay $\Delta T_{2,1}^s$ in the strong-field regime, due to the hairy black hole in Horndeski gravity and compared them to the Schwarzschild ($q = 0$) black hole of GR. We found that $\bar{a}$ and u_{ps} increase monotonically with increasing magnitude of q while $\bar{b}$ first increases, reaching its maximum at $q \approx -0.45$, and then decreases. The numerical values, in our selected range of q, are positive for $\bar{a}$ while negative for $\bar{b}$. We found that deflection angle α_D, for fixed impact parameter u, is greater for the hairy black hole in Horndeski gravity when compared to the Schwarzschild black hole and increases with the increasing magnitude of q. Also, the photon sphere radius x_{ps} increases with decreasing q, making bigger photon spheres in the hairy black hole in Horndeski gravity when compared to the Schwarzschild black holes of GR.

We calculated lensing observables θ_∞, s and r_{mag} of the relativistic images for supermassive black holes, namely, Sgr A*, M87*, NGC 4649 and NGC 1332 by considering the spacetime to be described by the hairy black hole in Horndeski gravity. In its predictions for gravitational lensing due to supermassive black holes, Horndeski gravity exhibits potentially observable departures from GR. The presence of parameter q rapidly increases θ_∞ and s when compared to the Schwarzschild ($q = 0$) black hole. We observe that θ_∞ ranges between 26.33 and 51.52 μas for Sgr A* and its devi-

ation from its GR counterpart can reach as much as 25.1912 μas while as for M87* it ranges between 19.78 and 38.71 μas and deviation is as high as 18.92μas. On the other hand the seperation s due to hairy black holes for Sgr A* and M87* range between 0.0329 and 1.15426 μas and 0.024 and 0.867 μas, respectively. In the limit, $q \to 0$, our results reduce exactly to the Schwarzschild black hole results. The angular positions of images though are very insensitive to the position of the source β with $\theta_{1p} > |\theta_{1s}|$ at higher values. θ_{1p} and θ_{2p}, which are the angular positions of first and second order primary images are 7.8 μas and 7.6 μas larger than their corresponding values in GR at $q = -0.5$. The first order images in Horndeski gravity are highly magnified than the corresponding images in GR. However, r_{mag} rapidly decreases with q suggesting that the Schwarzschild images are brighter than the hairy black holes in Horndeski gravity. Finally, the time delay of the first and second order images for hairy black holes in Horndeski gravity is significantly larger (e.g. $\sim$ 4758.1 min for M87*) than the GR counterparts for astronomical measurements, provided we have enough angular resolution separating two relativistic images, except for Sgr A* for which the deviation is $\sim$ 3.32 min; an effect too tiny to be detected by EHT.

We have also investigated strong deflection gravitational lensings by the Horndeski black holes and compared observable signatures with those of the neutral Horndeski, Galileon and charged Horndeski black holes via observation of the supermassive black holes M87* and SgrA*. It may provide hints for distinguishing these black holes and that it is possible to detect some effects of the strong deflection lensing by the hairy Horndeski black holes and other black holes with the EHT observations, but it is unconvincing to discern these black holes as deviations are too small, i.e., $\mathcal{O}(\mu\mathrm{as})$.

Many interesting avenues are amenable for future work from the hairy black holes in Horndeski gravity; most importantly is to consider the rotating black holes as there is observational evidence that black holes rotate. Our results will certainly be different in this case, and likely substantively for near-extremal solutions. Also, it will be interesting to analyze the relationship between the null geodesics and thermodynamic phase transition in AdS background in the context photon sphere. Further, gravitational lensing in the strong field may open fascinating perspectives for testing modified theories of gravity and estimating the parameters associated with the supermassive black holes.

References

1. S. Liebes, J. Phys. Rev. B **133**, 835 (1964)
2. S. Refsdal, Mon. Not. R. Astron. Soc. **128**, 295 (1964)
3. R.R. Bourassa, R. Kantowski, T.D. Norton, Astrophys. J. **185**, 747 (1973)
4. K.S. Virbhadra, G.F.R. Ellis, Phys. Rev. D **62**, 084003 (2000)
5. S. Frittelli, E.T. Newman, Phys. Rev. D **59**, 124001 (1999)
6. V. Bozza, Phys. Rev. D **66**, 103001 (2002)
7. E.F. Eiroa, D.F. Torres, Phys. Rev. D **69**, 063004 (2004)
8. R. Whisker, Phys. Rev. D **71**, 064004 (2005)
9. E.F. Eiroa, Phys. Rev. D **71**, 083010 (2005)
10. E.F. Eiroa, Braz. J. Phys. **35**, 1113 (2005)
11. G. Li, B. Cao, Z. Feng, X. Zu, Int. J. Theor. Phys. **54**, 3103 (2015)
12. A. Bhadra, Phys. Rev. D **67**, 103009 (2003)
13. K. Sarkar, A. Bhadra, Class. Quantum Gravity **23**, 6101 (2006)
14. W. Javed, R. Babar, A. Övgün, Phys. Rev. D **99**, 084012 (2019)
15. R. Shaikh, P. Banerjee, S. Paul, T. Sarkar, Phys. Rev. D **99**, 104040 (2019)
16. S. Chen, J. Jing, Phys. Rev. D **80**, 024036 (2009)
17. E.F. Eiroa, C.M. Sendra, Class. Quantum Gravity **28**, 085008 (2011)
18. A. Övgün, Phys. Rev. D **99**, 104075 (2019)
19. S. Panpanich, S. Ponglertsakul, L. Tannukij, Phys. Rev. D **100**, 044031 (2019)
20. X. Lu, Y. Xie, Eur. Phys. J. C **81**, 627 (2021)
21. K. Bronnikov, K. Baleevskikh, Gravit. Cosmol. **25**, 44 (2019)
22. R. Shaikh, P. Banerjee, S. Paul, T. Sarkar, Phys. Lett. B **789**, 270 (2019)
23. G.Z. Babar, F. Atamurotov, S. Ul Islam, S.G. Ghosh, Phys. Rev. D **103**, 084057 (2021)
24. R. Kumar, S.U. Islam, S.G. Ghosh, Eur. Phys. J. C **80**, 1128 (2020)
25. S.U. Islam, R. Kumar, S.G. Ghosh, JCAP **09**, 030 (2020)
26. B. Narzilloev, S. Shaymatov, I. Hussain, A. Abdujabbarov, B. Ahmedov, C. Bambi, Eur. Phys. J. C **81**, 849 (2021)
27. N. Tsukamoto, Phys. Rev. D **104**, 064022 (2021)
28. K. Akiyama et al., [Event Horizon Telescope], Astrophys. J. Lett. **875**, L1 (2019)
29. K. Akiyama et al., [Event Horizon Telescope], Astrophys. J. Lett. **875**, L4 (2019)
30. S.E.P. Bergliaffa, R. Maier, N.D. Silvano, arXiv:2107.07839 [gr-qc]
31. G.W. Horndeski, Int. J. Theor. Phys. **10**, 363 (1974)
32. T. Damour, G. Esposito-Farese, Class. Quantum Gravity **9**, 2093 (1992)
33. M. Horbatsch, H.O. Silva, D. Gerosa, P. Pani, E. Berti, L. Gualtieri, U. Sperhake, Class. Quantum Gravity **32**, 204001 (2015)
34. A. Nicolis, R. Rattazzi, E. Trincherini, Phys. Rev. D **79**, 064036 (2009)
35. T. Clifton, P.G. Ferreira, A. Padilla, C. Skordis, Phys. Rep. **513**, 1 (2012)
36. T. Kobayashi, Rep. Prog. Phys. **82**, 086901 (2019)
37. A. Maselli, H.O. Silva, M. Minamitsuji, E. Berti, Phys. Rev. D **93**, 124056 (2016)
38. R. Kase, S. Tsujikawa, Int. J. Mod. Phys. D **28**, 1942005 (2019)
39. M. Rinaldi, Phys. Rev. D **86**, 084048 (2012)
40. E. Babichev, A. Fabbri, JHEP **07**, 016 (2014)
41. E. Babichev, C. Charmousis, A. Lehébel, JCAP **04**, 027 (2017)
42. A. Anabalon, A. Cisterna, J. Oliva, Phys. Rev. D **89**, 084050 (2014)
43. A. Cisterna, C. Erices, Phys. Rev. D **89**, 084038 (2014)
44. M. Bravo-Gaete, M. Hassaine, Phys. Rev. D **90**, 024008 (2014)
45. T.P. Sotiriou, S.Y. Zhou, Phys. Rev. Lett. **112**, 251102 (2014)
46. T.P. Sotiriou, S.Y. Zhou, Phys. Rev. D **90**, 124063 (2014)
47. E. Babichev, C. Charmousis, A. Lehébel, Class. Quantum Gravity **33**, 154002 (2016)
48. R. Benkel, T.P. Sotiriou, H. Witek, Class. Quantum Gravity **34**, 064001 (2017)
49. J. Khoury, M. Trodden, S.S.C. Wong, JCAP **11**, 044 (2020)
50. L. Hui, A. Nicolis, Phys. Rev. Lett. **110**, 241104 (2013)
51. J. Badía, E.F. Eiroa, Eur. Phys. J. C **77**, 779 (2017)
52. M. Rinaldi, Phys. Rev. D **86**, 084048 (2012)
53. A. Cisterna, C. Erices, Phys. Rev. D **89**, 084038 (2014)
54. A. Anabalon, A. Cisterna, J. Oliva, Phys. Rev. D **89**, 084050 (2014)
55. T. Kobayashi, N. Tanahashi, Prog. Theor. Exp. Phys. **2014**, 073E02 (2014)
56. C. Charmousis, T. Kolyvaris, E. Papantonopoulos, M. Tsoukalas, J. High Energy Phys. **07**, 085 (2014)
57. M. Minamitsuji, Phys. Rev. D **89**, 064017 (2014)
58. E. Babichev, C. Charmousis, M. Hassaine, JCAP **05**, 031 (2015)
59. S.S. Zhao, Y. Xie, JCAP **07**, 007 (2016)
60. C.Y. Wang, Y.F. Shen, Y. Xie, JCAP **04**, 022 (2019)
61. R. Penrose, Riv. Nuovo Cim. **1**, 252 (1969)
62. S. Chandrasekhar, (Oxford University Press, New York, 1992)
63. V. Bozza, S. Capozziello, G. Iovane, G. Scarpetta, Gen. Relativ. Gravit. **33**, 1535 (2001)
64. K.S. Virbhadra, Phys. Rev. D **79**, 083004 (2009)
65. S.U. Islam, J. Kumar, S.G. Ghosh, JCAP **10**, 013 (2021)
66. V. Bozza, L. Mancini, Gen. Relativ. Gravit. **36**, 435 (2004)
67. T. Johannsen, D. Psaltis, Astrophys. J. **718**, 446 (2010)
68. T. Johannsen, Astrophys. J. **777**, 170 (2013)
69. L. Medeiros, D. Psaltis, F. Özel, Astrophys. J. **896**, 7 (2020)
70. D. Psaltis et al., [Event Horizon Telescope], Phys. Rev. Lett. **125**, 141104 (2020)
71. R. Kumar, A. Kumar, S.G. Ghosh, Astrophys. J. **896**, 89 (2020)
72. R. Kumar, S.G. Ghosh, Astrophys. J. **892**, 78 (2020)
73. P. Kocherlakota et al., [Event Horizon Telescope], Phys. Rev. D **103**, 104047 (2021)